# Synthesis of MoS$_2$-Au Nanocomposite Films by Sputter Deposition

Ronald S. Goeke, Somuri V. Prasad, Thomas W. Scharf and Paul G. Kotula

**Sandia National Laboratories**

# Synthesis of MoS$_2$-Au Nanocomposite Films by Sputter Deposition

Ronald S. Goeke, 1832
Advanced Prototyping S&T

Paul G. Kotula, 1822
Materials Characterization

Somuri V. Prasad, 1831
Multiscale Metallurgical S&T

Sandia National Laboratories
P.O. Box 5800
Albuquerque, New Mexico  87185

Thomas W. Scharf
University of North Texas

**Abstract**

Molybdenum disulfide based solid lubricants, which are well known for their lubricating behavior in dry and inert atmospheres, oxidize in humid environments.  This study focuses on the synthesis of Au doped MoS$_2$ nanocomposite thin films created by co-sputter deposition at various temperatures for environmental robustness. The ratio of the deposition flux was adjusted to control the composition to about 10% Au by weight.  (Scanning) transmission electron microscopy (S)TEM revealed that the room temperature deposited nanocomposite consisted of 2-4 nm size Au particles in a matrix of semi-crystalline MoS$_2$. With increasing growth temperatures, the nanocomposite exhibited structural changes: the Au nanoparticles coarsened by diffusion-driven Ostwald ripening to 5-10 nm size and the MoS$_2$ basal planes encapsulated the Au nanoparticles thereby forming a novel solid Au core MoS$_2$ nano-onion like structures.  *In situ* TEM heating revealed that Au nanoparticles also coarsened, but unlike heating during film growth, the highly ordered basal planes did not encapsulate the Au.  Friction and wear tests confirmed that the MoS$_2$-Au nanocomposite films grown at elevated temperatures had significantly longer wear life in air with 50% RH as compared with pure MoS$_2$.  During frictional contact, exfoliation of the MoS$_2$ basal planes occurred parallel to the sliding direction, providing a thin blanket of lubrication.  All the films were found to be deficient in sulfur.  Studies during the final phase of the project indicate that near stoichiometric films can be grown by introducing a small dose of H$_2$S gas during sputtering.

# ACKNOWLEDGMENTS

# CONTENTS

# FIGURES

# TABLES

# 1. INTRODUCTION

Transition metal dichalcogenides, most notably molybdenum disulfide ($MoS_2$) and tungsten disulfide ($WS_2$), are well known for their solid lubricating behavior [1-10]. In the $MoS_2$ layered structure, a sheet of molybdenum atoms is sandwiched between two hexagonally packed sulfur layers as shown in Figure 1-1. The bonding within the S-Mo-S sandwich is covalent, while weak Van der Waals forces exist between adjacent sandwiches, resulting in interlamellar mechanical weakness.
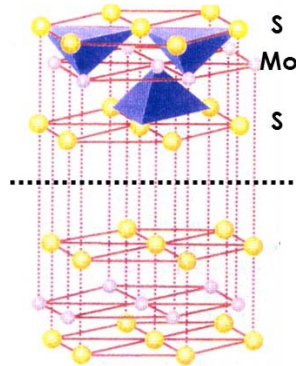


**Figure 1-1 –MoS$_2$ hexagonal close packed lamellar structure**

Thus, under a shearing force the basal planes slide over one another by intracrystalline slip and transfer to the rubbing counterface. These mechanisms for imparting low interfacial shear [1-4, 11] are: a) the development of a transfer film on the counterface to accommodate interfacial sliding, and b) reorientation, or creation, of the (0002) basal plane parallel to the sliding direction in the wear track. The low friction coefficients of the pure $MoS_2$ and $WS_2$ coatings are only exhibited in either dry inert gas or in ultrahigh vacuum [11-13]. Conversely, interfacial sliding in air results in a higher coefficient of friction [Figure 1-2] and significantly reduced wear life.
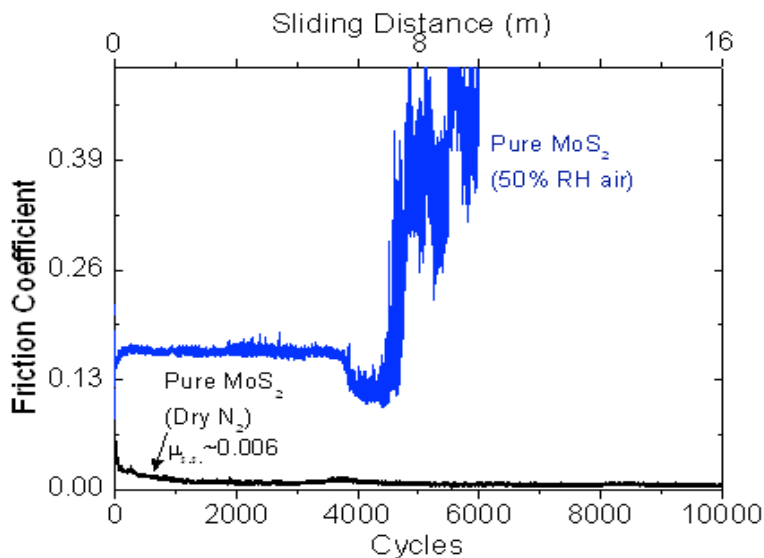


**Figure 1-2 – MoS$_2$ frictional behavior in dry or humid environments (subscript "s.s." in Figure corresponds to "steady state")**

It is believed that dangling or unsaturated bonds on the edge of basal planes react with moisture and oxygen in the environment leading to higher friction and the eventual coating failure. The edge plane oxidation or corrosion is schematically depicted in Figure 1-3. The water vapor reacts with the molybdenum disulfide generating molybdenum oxide and hydrogen sulfide gas. This is the rotten egg smell that is frequently observed around $MoS_2$ films that have been improperly stored.
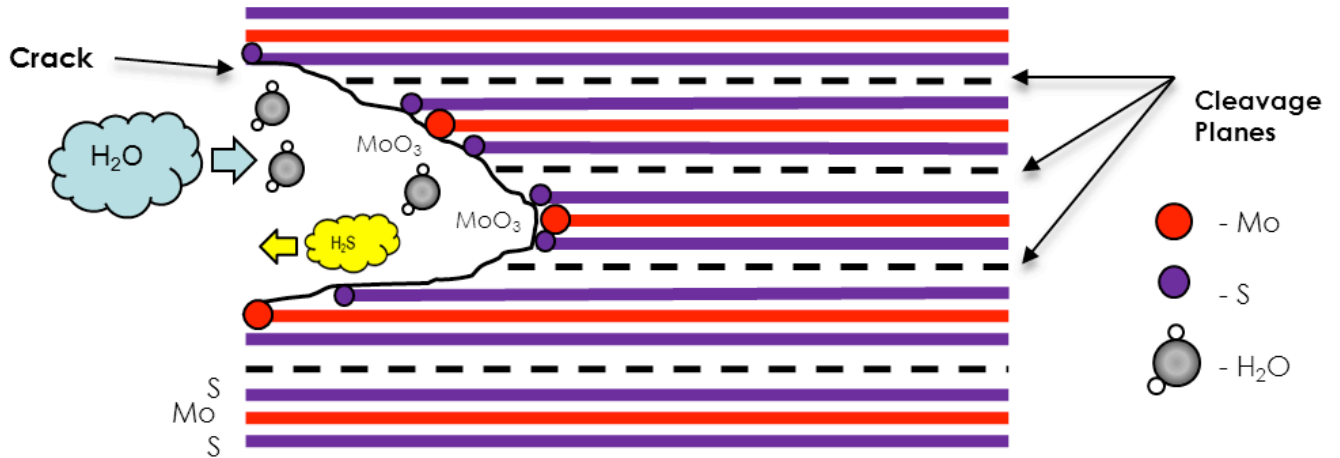


**Figure 1-3 – Moisture attack of MoS₂ edge planes [14]**

There is an increasing demand for environmentally robust solid lubricant coatings that can adapt themselves to different environments. For instance, even if the targeted application is friction mitigation in hermetically sealed devices backfilled with dry nitrogen, any compromise in the hermeticity during dormancy and long term storage can potentially expose the moving mechanical assemblies to humidity. In view of this, there have been major studies aimed at developing multi-phase materials known as adaptive lubricants and chameleon coatings [15, 16]. A number of metal or oxide dopants in $MoS_2$ have also been successfully tried. Notable examples of dopants include: Ti [17-21], Al [22, 23], Ni [24-26], Au [8, 24, 26], Pb [24, 27, 28], PbO [24, 29, 30], $Sb_2O_3$ [25, 30-35]. The presence of these dopants can lead to increased coating density, hardness, and oxidation resistance. However, some of these doped films, specifically the $Sb_2O_3$ doped $MoS_2$ tend to be brittle leading to fracture and delamination.

The major objective of this study was to explore the feasibility of synthesizing $MoS_2$-Au nanocomposite by dual-gun magnetron sputtering deposition system capable of simultaneously ablating materials from two different targets. Additionally, the PVD system was interfaced with a hot stage. Unlike the previous studies, i.e., the one referred to above or previous Sandia studies, the in-situ specimen heating enabled the synthesis of films with novel nanostructures. A secondary objective was to characterize the friction behavior in different environments.

# 2. SYNTHESIS OF NANO-COMPOSITES

Physical Vapor Deposition or PVD is a vacuum deposition process in which a thin film is generated from the condensation of a vaporized form of the target material. Sputter deposition is a form of PVD in which a glow discharge plasma, typically of argon, bombards the target generating material vaporization or "sputtering" from kinetic energy. This is an energetic process resulting in not only sputtered molecules, but also atoms and other dissociated molecular fragments. This energetic vapor gives up its energy and condenses upon collision with cold surfaces as schematically depicted in Figure 2-1. The $MoS_2$ and $MoS_2$-Au films were deposited by this process.
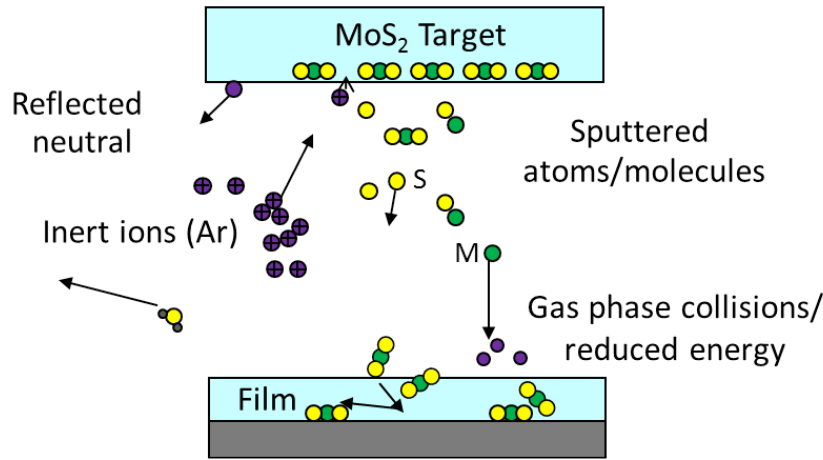


**Figure 2-1  Sputter Deposition Process**

The films in this study were grown in a custom built PVD system designed for sputter co-deposition. The system has two 2" cathodes (Angstrom Sciences OYNX 2") located at 90° angles to each other. The rotatable substrate holder is at a 45° angle to each target, so that the deposition flux from both targets arrives simultaneously on the Si (001) or 1308 steel substrates. One of the targets was pure $MoS_2$ (Materion Advanced Chemical) and the other was pure Au (Materion Advanced Chemical) fabricated to >99.999% purity. The deposition rate for each material was controlled by two independent quartz crystal microbalances (QCM). The QCMs were adapted with line of sight tubes to eliminate cross-talk. The tooling factors for the QCMs were generated separately using a stylus profilometry of the deposited film. Figure 2-2 shows a schematic and a picture of this deposition system.
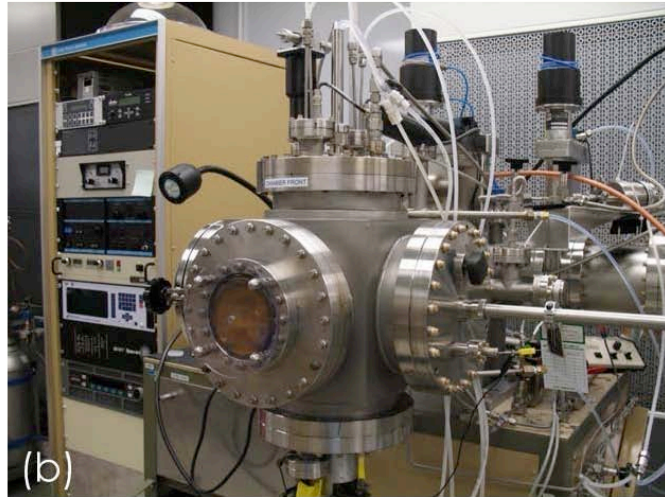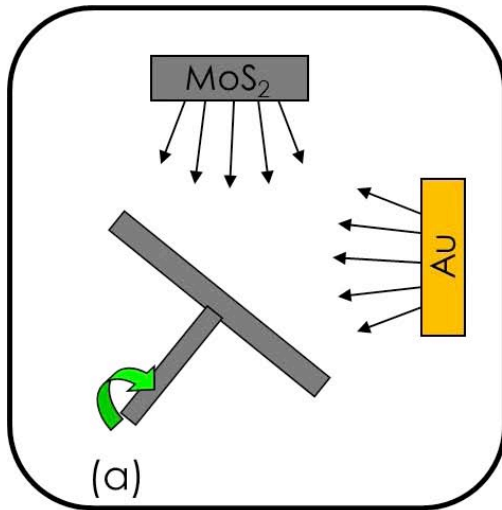
**Figure 2-2 – A schematic (a) and a photograph (b) of the PVD Co-Deposition system**

A radio frequency (RF) power supply was used to deposit from the Au target mounted on a 2"
magnetron. The RF power was used to enable a lower Au deposition rate. The $MoS_2$ material
was deposited using a pulsed DC power supply. The pulsed DC power was a 5KW Advanced
Energy Pinnacle in-line with an Advanced Energy Sparkle pulse generator. The deposition
parameters used are shown in Table 1 and include ~20W RF power on the gold target, but was
adjusted to maintain the desired 10% gold in the final film composition. The sputter gas was
pure Argon at a flow rate of ~50 sccm. These conditions resulted in a deposition rate of ~7 Å/s.
The cryo-pumped system achieved a base pressure < 5 x $10^{-5}$ Pa prior to starting the deposition.

**Table 1.  Deposition Process Conditions**

| | |
|---|---|
| Targets Size (diameter) | 50 mm |
| DC Cathode Power      $MoS_2$ | 160 watts |
| Distance target-substrate | 125 mm |
| Pressure (base) | < 5x$10^{-5}$ Pa |
| Pressure (deposition) | 0.73 Pa |

Photographs of the system revealing the features inside this custom deposition chamber are
shown in Figure 2-3(a). The system has the capability to heat the substrate to 400°C, using a
backside coil heater from Watlow. Each of the two magnetron cathodes has the option of either
RF or DC power. A minimum power of 15 watts is required to ignite and maintain a glow
discharge. This minimum power required for ignition sets the lower limit for the deposition rate.
The rotating substrate stage is electrically isolated and can be DC biased up to -300V. The QCM
monitors with their line of sight tubes are also visible, which enable independent real time
control over composition.
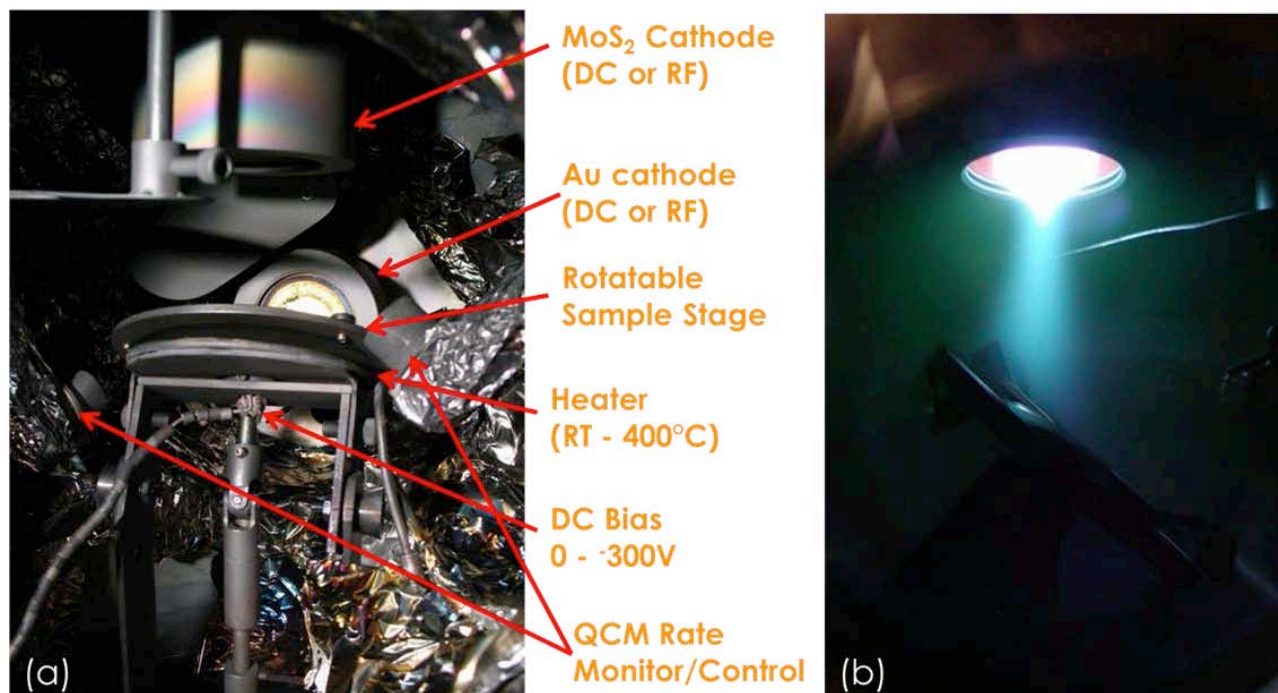
**Figure 2-3 – View inside co-deposition chamber**

The glow discharge visible in Figure 2-3(b) on the $MoS_2$ target is primarily concentrated near the sputter target (cathode) but visibly extends down to the substrate (anode). While the generation of sputter material, in our case the $MoS_2$, occurs at the target, the plasma extends all the way to the substrate, which is adding energy to the growing film by bombardment of positive ions.

# 3.  CHARACTERIZATION

The coatings were characterized by high resolution scanning electron microscopy (HRSEM); cross-sectional transmission electron microscopy (XTEM) with energy-dispersive x-ray spectrometry (EDXS) and selected area electron diffraction (SAED).  High-angle annular dark field scanning transmission electron microscopy (HAADF-STEM) was also used for Z-contrast imaging.  TEM specimens were prepared with a FEI DB-235 dual-beam focused ion beam microscope (FIB), and then analyzed in a FEI Tecnai F30-ST TEM/STEM operated at 300kV and equipped with EDXS.  Friction-induced changes to the microstructure and crystallography in the subsurface regions were analyzed from cross-sectional TEM analysis of wear surfaces generated from the friction and wear tests.  Site specific FIB samples were taken in the center of the wear surface and along the direction of sliding.  To protect the wear surfaces from ion beam damage, wear surfaces were first coated with carbon and platinum prior to FIB milling. Carbon coating also provided a clear z-contrast between the wear surface and the top protective Pt.

## 3.1.     Plan view SEM

A pure $MoS_2$ thin film has been imaged by Scanning Electron Microscopy (SEM) and is shown in Figure 3-1(a).  In this micrograph the high amount of porosity in the film can be clearly observed for this room temperature deposited film.  A nanocomposite thin film of co-sputtered $MoS_2$-Au, also deposited at room temperature, is shown in Figure 3-1(b).  The nanocomposite $MoS_2$-Au film exhibited significantly reduced porosity.  In the high resolution SEM image [Figure 3-2], the nano-particles of gold appear as bright dots in the SEM and are a few nanometers in size.
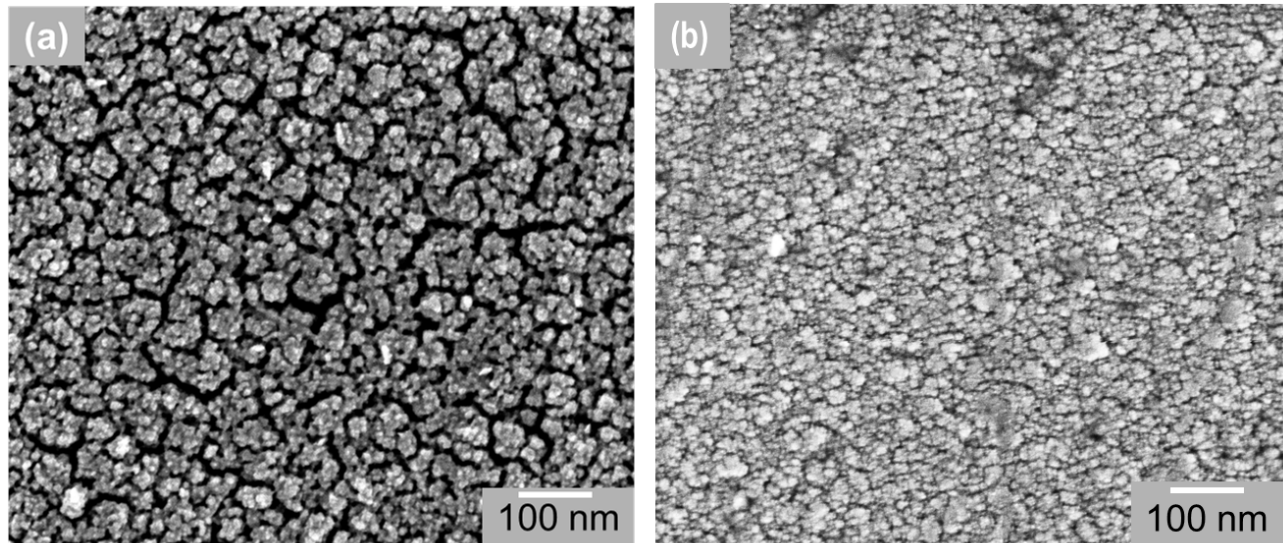


**Figure 3-1 - Plan view SEM of (a) Pure $MoS_2$ film and (b) $MoS_2$ - Au film deposited @ RT**
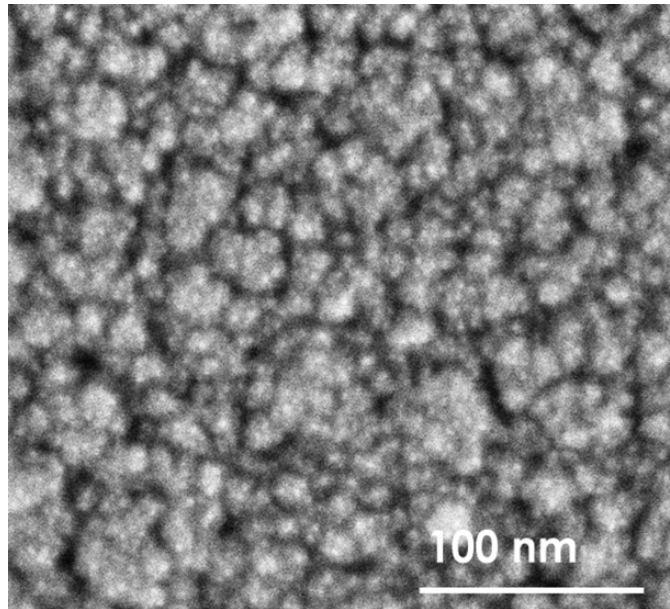
**Figure 3-2 – HRSEM of MoS$_2$-Au nanocomposite deposited @ RT**

## 3.2. Cross-sectional TEM
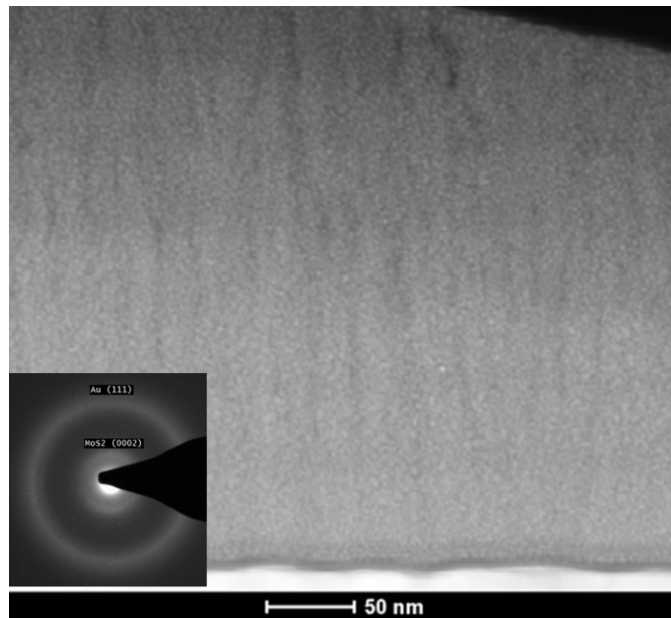


**Figure 3-3 - HAADF-STEM…nanocrystalline Au (~2nm) and MoS$_2$
Selected-area diffraction**

A typical STEM image of a cross section of the room temperature deposited MoS$_2$-Au film is shown in Figure 3-3. The diffuse rings in the selected area diffraction pattern in the inset indicate that the film has extremely fine crystallites and the crystallites are randomly oriented.
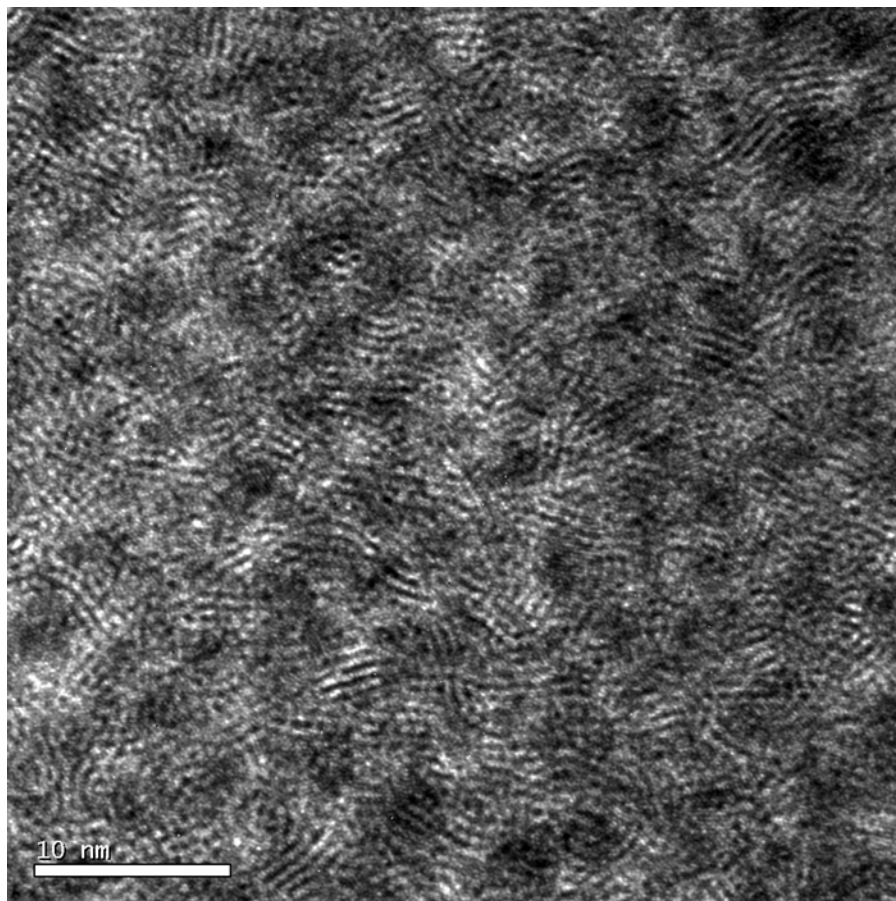
**Figure 3-4 – HRTEM of RT deposited MoS$_2$-Au nanocomposite**

Shown in Figure 3-4 is a cross-sectional Bright Field Transmission Electron Microscope (BFTEM) image of a Au-MoS$_2$ nanocomposite film deposited at room temperature and Figure 3-5 shows the Au-MoS$_2$ nanocomposite film as deposited at 200°C. The dark regions are nanocrystalline Au, which seemed to coarsen from ~2 to ~10 nm compared with the room temperature deposited ones. This Au nanoparticle coarsening likely occurs by a diffusion-driven Ostwald ripening process. The surrounding MoS$_2$ basal lattice planes (~2 nm domain size) tend to wrap around the Au nanoparticles by forming a partially closed MoS$_2$ shell. A typical 10nm sized gold particle partially enclosed by a multi-walled MoS$_2$ basal plane shell is shown in Figure 3-5.
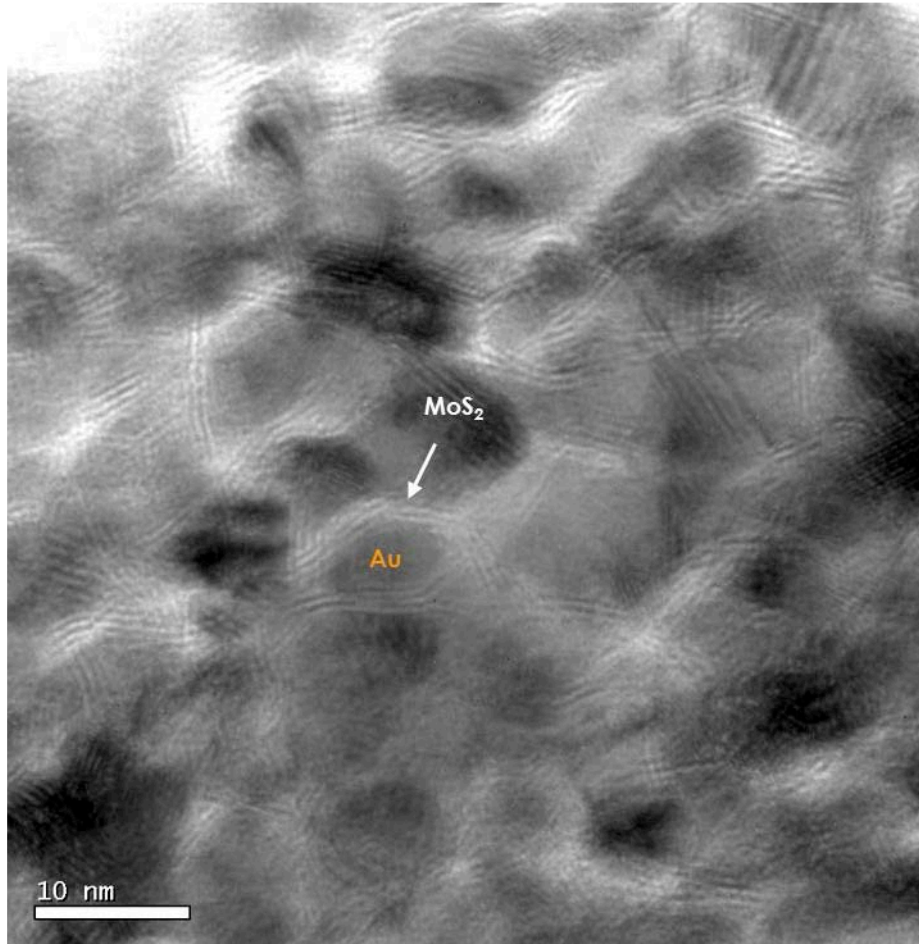
**Figure 3-5 – Cross-sectional BFTEM image of a 200°C deposited MoS$_2$-Au nanocomposite.**

The phenomenon observed here, namely the formation of these novel nanostructures is analogous to previous studies by Tenne and co-workers on inorganic fullerene structures [36, 37]. The authors pioneered the synthesis of inorganic fullerene metal dichalcogenides, e.g. IF-MoS$_2$ and IF-WS$_2$. They have also synthesized IF with solid core MoO$_2$ nanoparticles (~35 nm size) encapsulated by MoS$_2$ layers [38]. The oxide core is progressively converted into the IF-MoS$_2$ within 30–90 min of annealing in an H$_2$S atmosphere.

These novel nanostructures were only observed in films deposited at substrate temperatures of 200 to 300°C. The combination of surface temperature and kinetic energy from the plasma is required for their formation. At low temperatures the MoS$_2$ is nano-crystalline and at higher temperatures the gold particles become very large due to sintering.

## 3.3.    Aberration Corrected TEM

Atomic-resolution high-angle annular dark-field STEM images were acquired with an FEI Titan™ G2 80-200 with ChemiSTEM™ technology (X-FEG™ and SuperX™ SDD array), operated at 200kV and equipped with a CEOS D-COR probe spherical aberration corrector (correction of $3^{rd}$, $4^{th}$, and optimized $5^{th}$ order aberrations). The images show Z-contrast in that heavier atomic columns such as Au are brighter than either Mo or S columns, Figure 3-6.
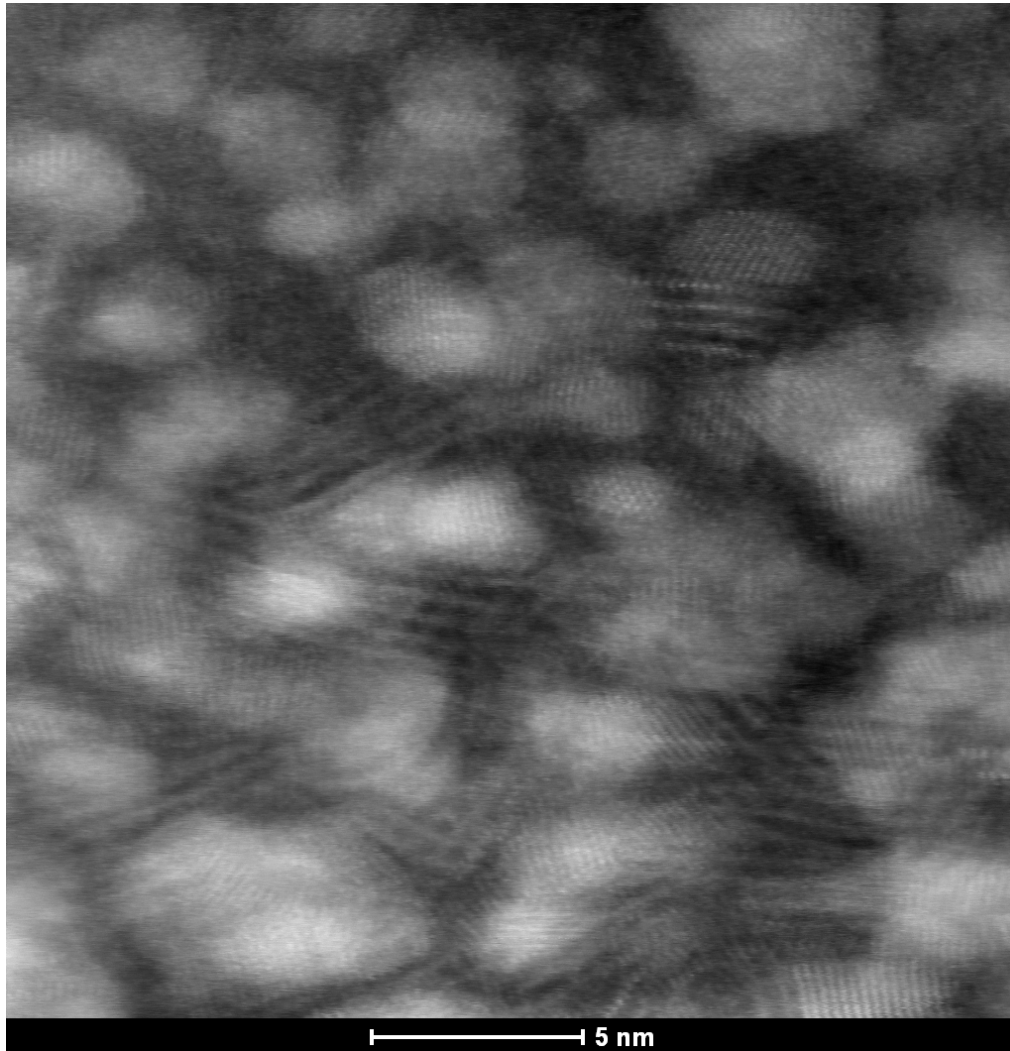


**Figure 3-6 – ACTEM – ADF micrograph of MoS$_2$-Au film grown at 100°C**

A close-up of the molybdenum and sulfur planes can be seen in Figure 3-7, where the molybdenum atoms are brighter than the sulfur atoms.  The large spacing between the sulfur-sulfur layers demonstrates the weak van der Waals bonding.  Also in this figure, the deposition of the MoS$_2$ layers appears to grow around the gold nanoparticle, with the sulfur atoms closest to the gold surface.
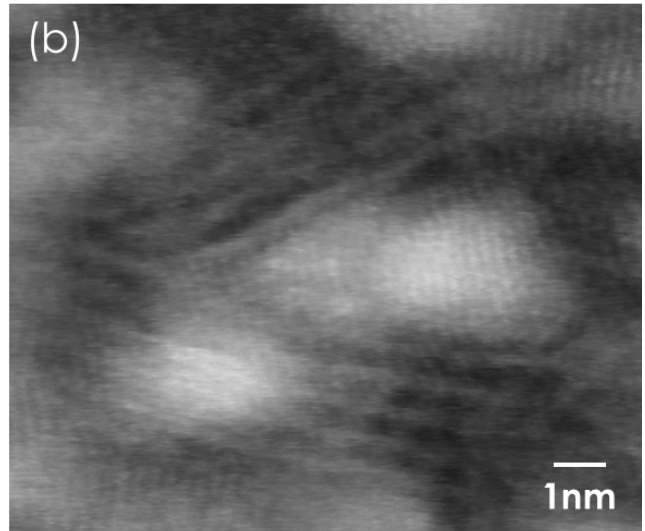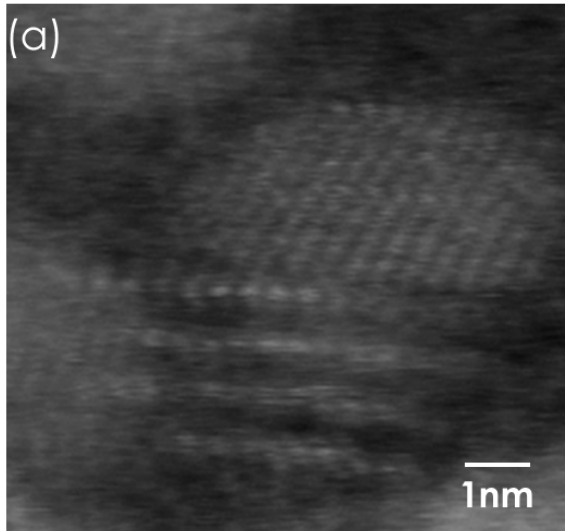
**Figure 3-7 – (a) Planes of Mo and S atoms layers with a c-plane spacing of 6.2Å and (b) MoS$_2$ layer formation around Au nanoparticles**

# 4. IN-SITU TEM HEATING EXPERIMENTS

Thermally-induced changes to these nanostructures were monitored by performing in-situ TEM experiments with a hot stage. The objective was to visualize whether wrapping of $MoS_2$ basal pales would occur in a room temperature deposited film if it was annealed at elevated temperatures. A thin FIB cross-sectioned TEM specimen of room temperature deposited $MoS_2$-Au film was mounted on a Protochips Aduro heater and the assembly was inserted into the TEM specimen chamber. This Aduro TEM grid has millisecond thermal ramp times allowing in situ rapid thermal annealing of the film to be observed. The imaging resolution and sample stability were better at room temperature so the sample was quickly brought to the desired temperature, held for 60 seconds and then quenched to room temperature and re-imaged. An image of the cross-section film on the TEM grid is shown in Figure 4-1.

Protochips Aduro in situ TEM heating stage
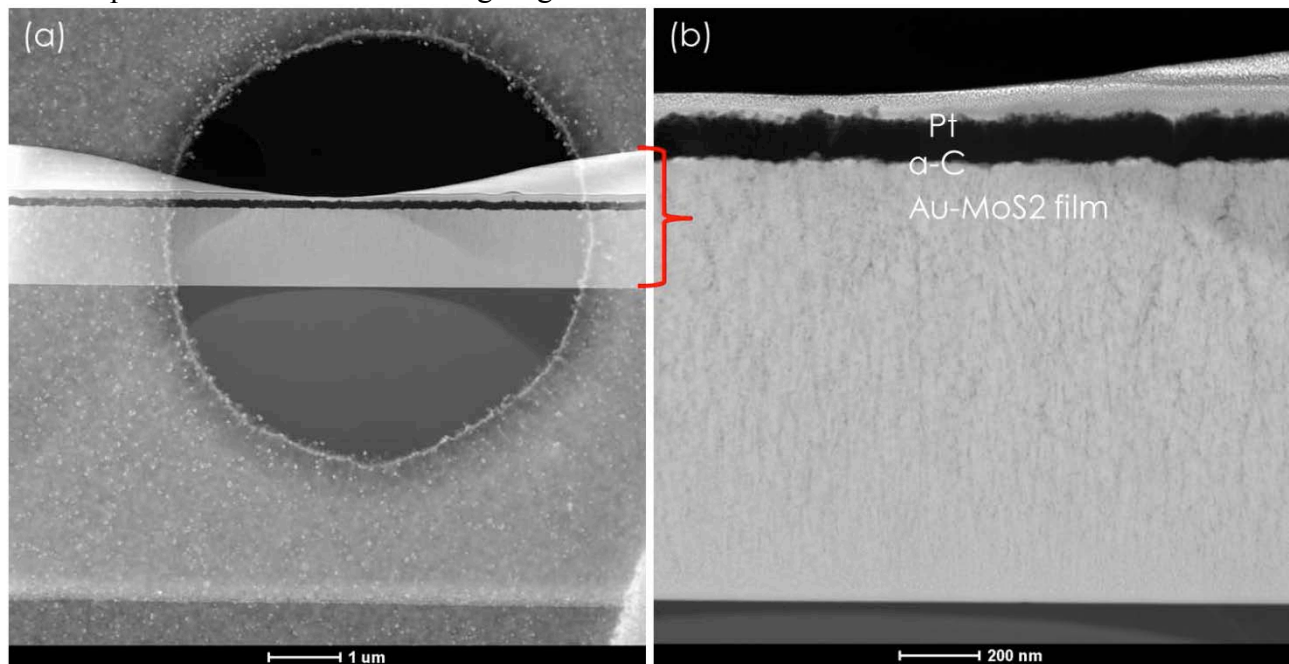


**Figure 4-1 – Protochips TEM grid with cross section sample over electron transparent opening**

This initial nanocrystalline film had 2nm grains of Au and $MoS_2$ and showed little change up to 200°C. In the High Angle Annular Dark Field (HAADF) mode the Au nanoparticles appear as bright particles in the image. The film, which exhibits some porosity as deposited, appears to undergo densification as the temperature is increased.

Figure 4-2 shows *in situ* TEM heating HAADF-STEM images with increasing temperature. The sequence shows that the Au nanoparticles coarsen (bright spots on the darker $MoS_2$ matrix) from 200 to 600°C. With increasing temperatures, larger Au nanoparticles grow at the expense of the smaller ones. The series of images in Figure 4-2 was collected upon cooling from the designated

higher temperature to room temperature, indicating that coarsening of Au nanoparticles is irreversible. The melting temperature of Au decreases significantly from its bulk value (1064°C) when particle dimensions are reduced to the nano-scale, an ~3 nm diameter Au particle can melt at temperatures as low as 500°C, due to the increase in the surface/volume ratio [39]. However, our particle size versus temperature data show that larger Au nanoparticles grow at the expense of the smaller ones in a solid-state, Ostwald-type ripening process before they reach the size-dependent melting points of isolated Au nanoparticles.

Similar in some respects to our work, Reich *et al [40]* studied how native Au nanoparticles with a mean diameter of 4 nm found in the mineral arsenian pyrite [Fe(S,As)$_2$], thermally evolved with *in situ* TEM heating to 650°C. They determined that above 370°C coarsening occurs by diffusion-driven Ostwald ripening. While we do not observe Au melting, the Au nanoparticle coarsening mechanism is similar.
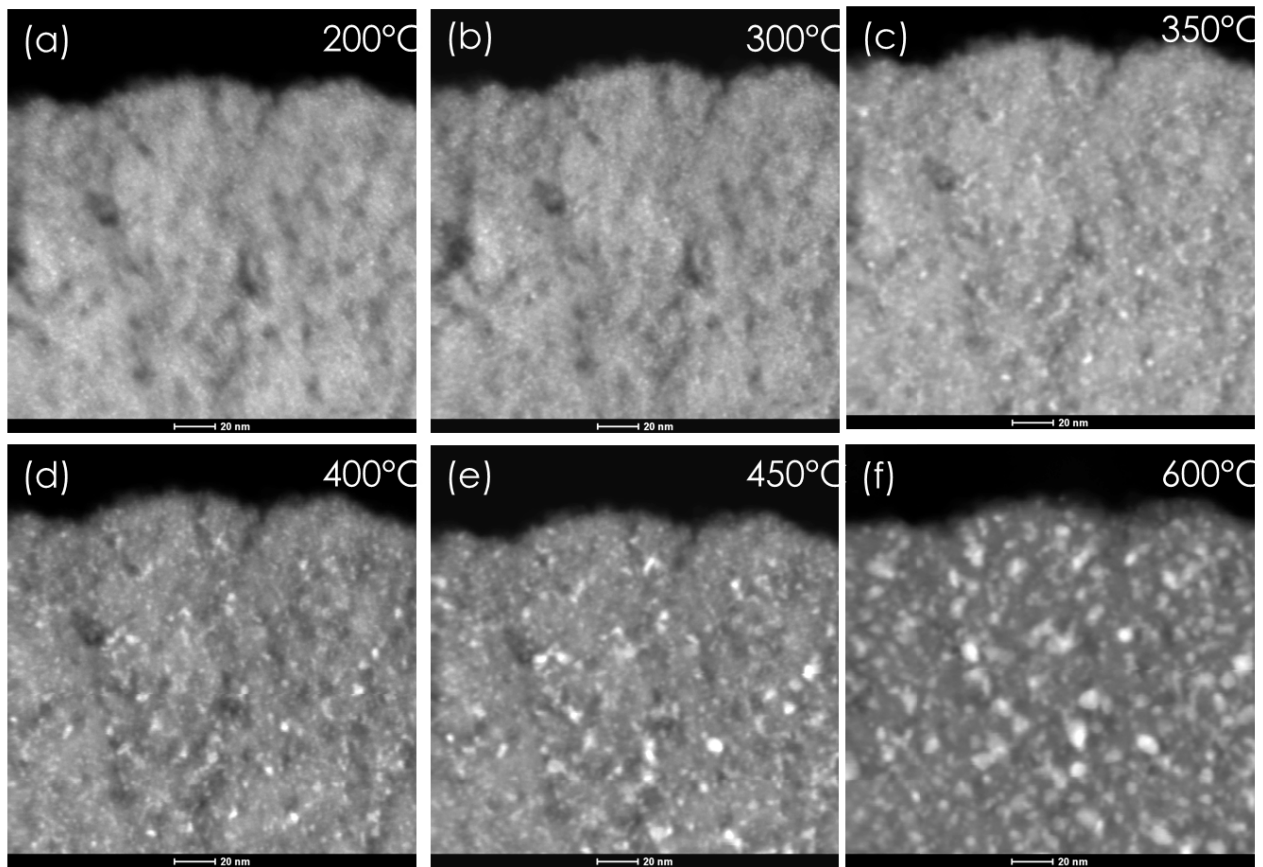


**Figure 4-2 – STEM/HAADF of MoS$_2$-Au nanocomposite during in situ heating**

Figure 4-3 shows the same film and process as Figure 4-2, but using High Resolution Transmission Electron Microscopy. In these images the Au nanoparticles are dark, but the growth of the MoS$_2$ crystalline phase is more apparent. The long range order of the MoS$_2$ planes, and crystallite size, grows significantly above 400°C.
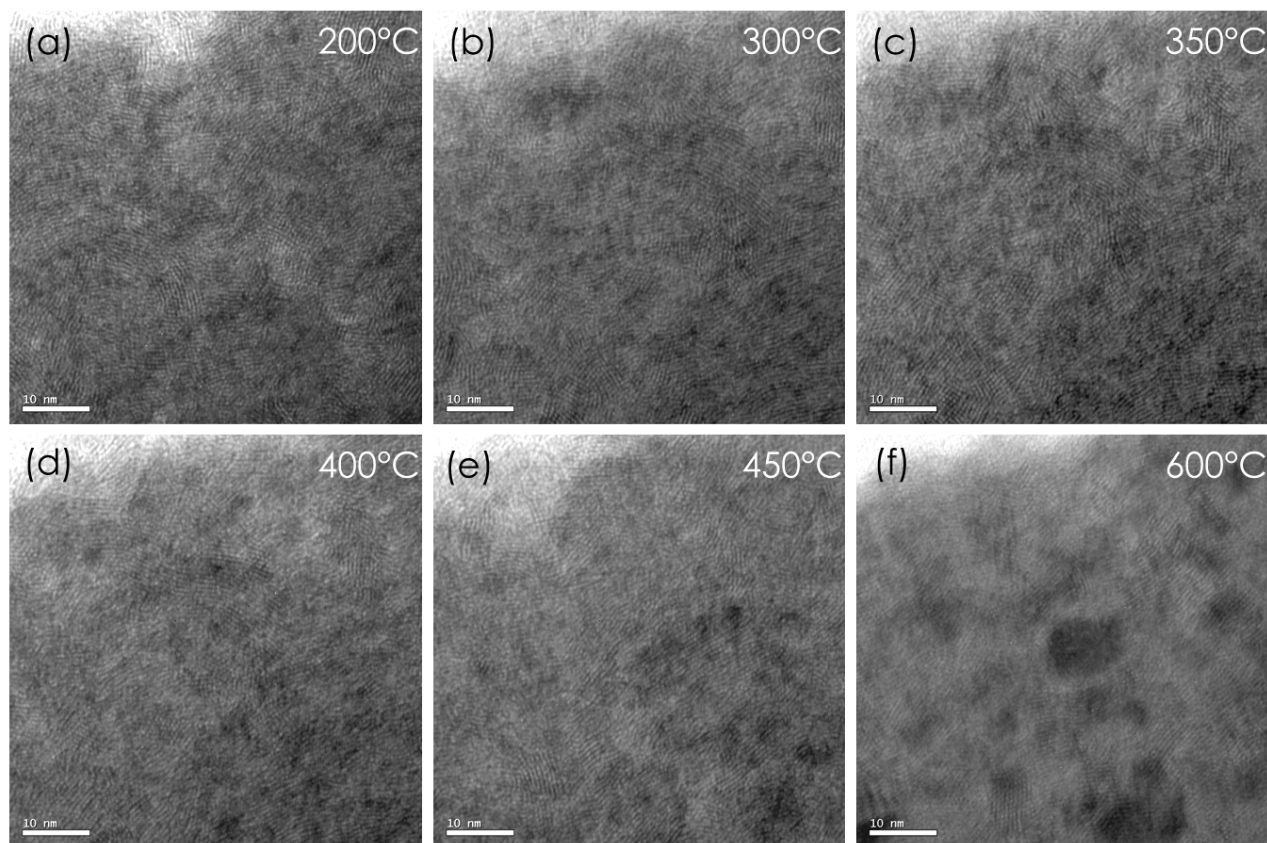
**Figure 4-3 – HRTEM of MoS$_2$-Au nanocomposite during in situ heating**

# 5. TRIBOLOGY

Friction measurements were made on planar surfaces using a ball-on-disk linear wear tester described in detail elsewhere [31]. The films were deposited on metallographically polished 13-8 steel coupons. The tests were performed in unidirectional sliding mode. Normal load (L) was applied by means of deadweights. A force transducer (Sensotec, Inc. Columbus, Ohio) in the load arm measured the friction load (F) over a track distance of 1.6 mm; the load cell has sensitivity to measure the tangential load of ~500 $\mu N$. The load cell was calibrated before each test. The sliding speed was 3.7 mm/s. The ratio of tangential to normal load is the friction coefficient. The tester was housed in an environmental chamber with precise control of dew point and oxygen content. Measurements were made in either dry nitrogen (< 10 ppm $O_2$ and < 100 ppm $H_2O$) or ambient air with 50% relative humidity (RH) environments. A 3.17 mm diameter $Si_3N_4$ ball (arithmetic average surface roughness, Ra, of 3 nm) was used as a counterface material on planar test coupons at normal loads ranging from 98 to 980 mN, which correspond to initial mean Hertzian contact stresses from 0.3 to 1.1 GPa, respectively. Friction and wear tests were run for either 1000 (short) or 10,000 (long) unidirectional cycles, and at least three measurements were made for each condition.
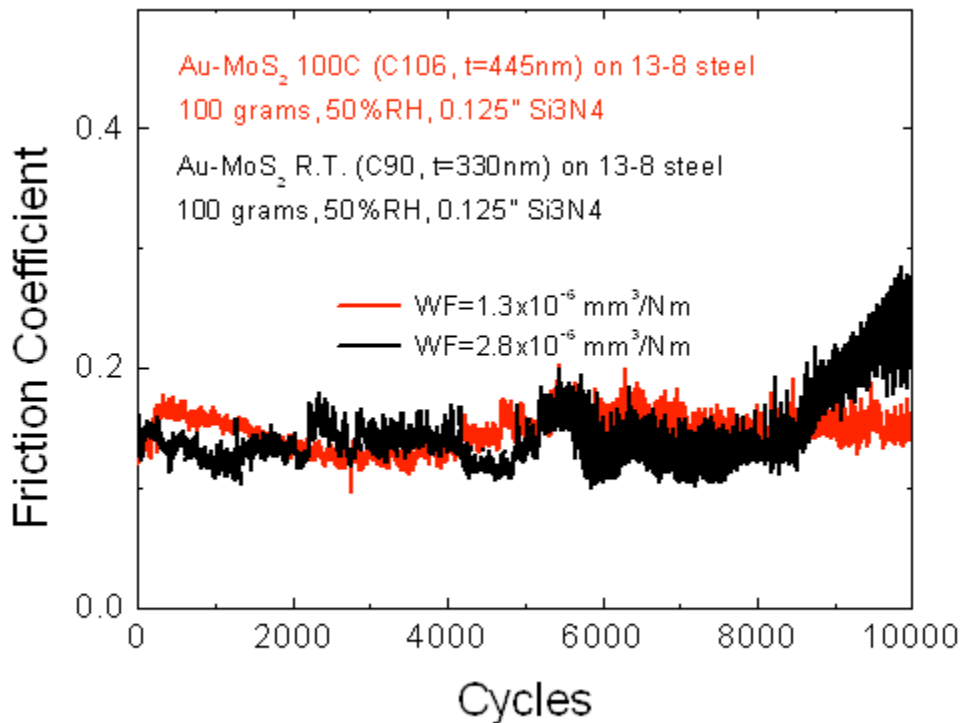


**Figure 5-1  Friction coefficients of MoS$_2$-Au composite films tested in air with 50% RH. The black line corresponds to the room temperature deposited film and the red curve represents the film deposited at 100ºC**

Friction coefficients of $MoS_2$-Au composite films tested in air with 50% RH are shown in Figure 5-1. Compared with the pure $MoS_2$ film [Figure 1-2], the composite films grown at 100ºC lasted the entire 10,000 cycle test with a COF of ~0.15. It is also worth noting that the wear factor (WF, i.e., volume of material removed per unit load and per unti sliding distance) the film grown at 100ºC ($1.3 \times 10^{-6}$ $mm^3$/Nm) is lower than the room temperature deposited one ($2.8 \times 10^{-6}$ $mm^3$/Nm).
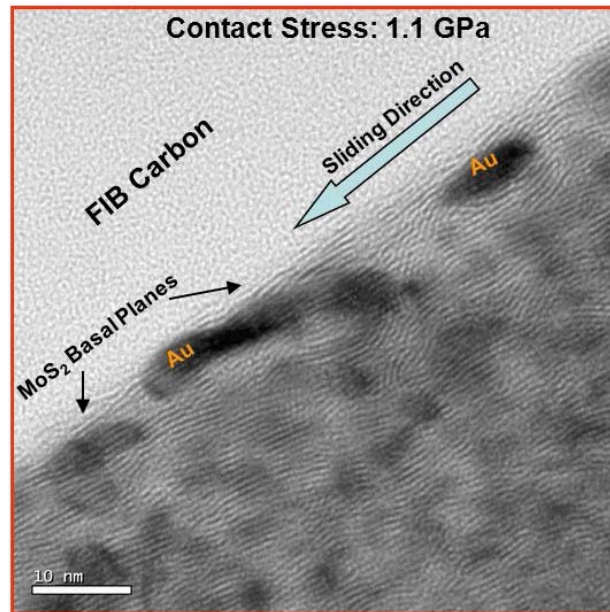


**Figure 5-2  High resolution STEM images of a cross-section of the wear scar**

A typical STEM image of a cross-section of the wear surface is shown in Figure 5-2. The arrow indicates the sliding direction. It is evident that frictional contact induced major changes to the structure of the film in the near and subsurface regions [Figure 3-5 and Figure 5-2]. The Au particles in the top layer coarsened significantly and are elongated in the direction of sliding. During frictional contact, exfoliation of the $MoS_2$ basal planes occurred parallel to the sliding direction, providing a thin blanket of lubrication. The interlamellar d-spacing between the top planes in Figure 5-2 was ~6 Å which compared well with the indexed 9PDF 01-087-2416) 6.1 Å lattice spacing for a $MoS_2$ lattice.

## 6. FILM STOICHIOMETRY

The film stoichiometry was characterized with a C ameca SX100 EPMA (Electron Probe MicroAnalyzer), also referred to as wavelength dispersive x-ray spectroscopy or WDS. T he results were analyzed with EPMA Enterprise Edition for Electron Probe Micro Analysis Software, Version 8.56. This software also runs all corrections. A pure single crystal $MoS_2$ was used as the compositional standard along with pure Au and silicon standards. Th e EPMA technique provides very good peak separation of molybdenum and sulfur as can be seen in Figure 6-1, which enable accurate measurements of the film composition.
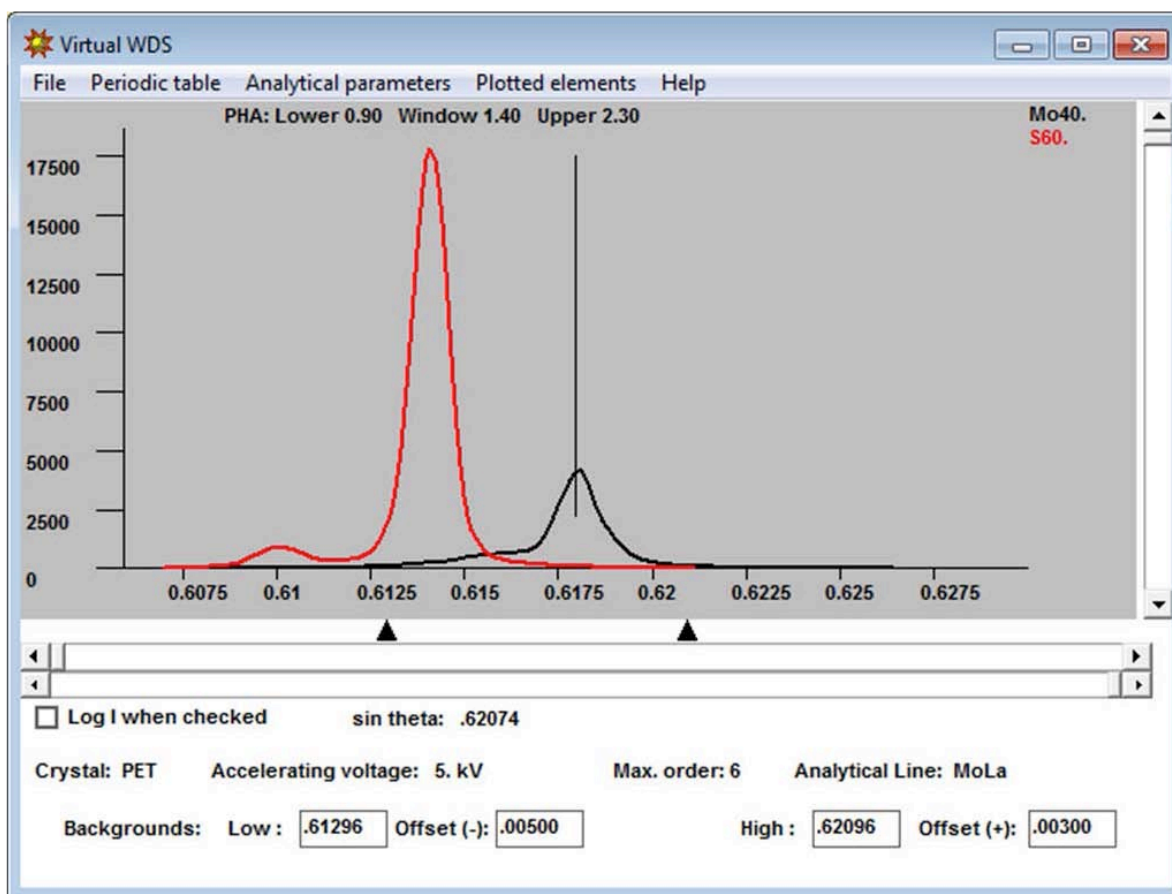
**Figure 6-1  A typical EPMA spectra for pure MoS$_2$**

The EPMA results are shown in Table 2.  The stoichiometry indicates that the films are sulfur deficient.  The ideal thermodynamically stable phase should have a S/Mo ratio of 2.0.  As described in Section 2, the sputter deposition process results in some decomposition of the starting MoS$_2$ molecule.  So the lower sulfur content is expected, as sulfur has a high vapor pressure (~3x10$^{-4}$ Pa at room temperature) and could be lost to the vacuum system during deposition.  An interesting result was that the composition of sulfur in the film increased with run number regardless of substrate temperature.  This appears to be related to the background sulfur available in the system as more deposition runs are completed.  This indicates that the conditioning of the system prior to growing a MoS$_2$ film could have a significant impact on the resulting film composition.  Sub-stoichiometric or sulfur deficiency is typical of almost all commercially produced physical vapor deposited MoS$_2$ thin films.

**Table 2 – EPMA Composition Results**

| Run# | Description | S/Mo Ratio | Wt% Au | Vol% Au |
|------|-------------|------------|--------|---------|
| C159 | MoS$_2$  RT | 1.558 | | |
| C160 | MoS$_2$-Au @ 300°C | 1.564 | 11.90% | 3.03% |
| C161 | MoS$_2$-Au @ 200°C | 1.571 | 8.32% | 2.13% |
| C162 | MoS$_2$-Au @ 100°C | 1.583 | 8.90% | 2.28% |
| C163 | MoS$_2$-Au @ RT | 1.597 | 9.83% | 2.51% |

One approach to mitigate substoichiometry is to introduce a small amount of $H_2S$ to the argon process gas. The plasma decomposition of the $H_2S$ provides a controllable amount of sulfur to the growing film.

The current vacuum system consisted of a cryo-pump for the high vacuum. This type of pump is known as a capture pump because the pumped gases are adsorbed onto the pump's cold array surfaces. During regeneration of a cryo-pump the adsorbed material is released by warming up the cryo-pump array. It would very dangerous to use this type of pump with a toxic gas such as $H_2S$. A turbo-molecular pump, which is a through type pump, was installed on the vacuum system. Also a vented gas cabinet for the $H_2S$ bottle was incorporated into the system to mitigate potential environmental safety and hazards. Photographs of these additions are shown in Figure 6-2, which combine to provide an engineered safe environment to process $MoS_2$ films with control over the stoichiometry.
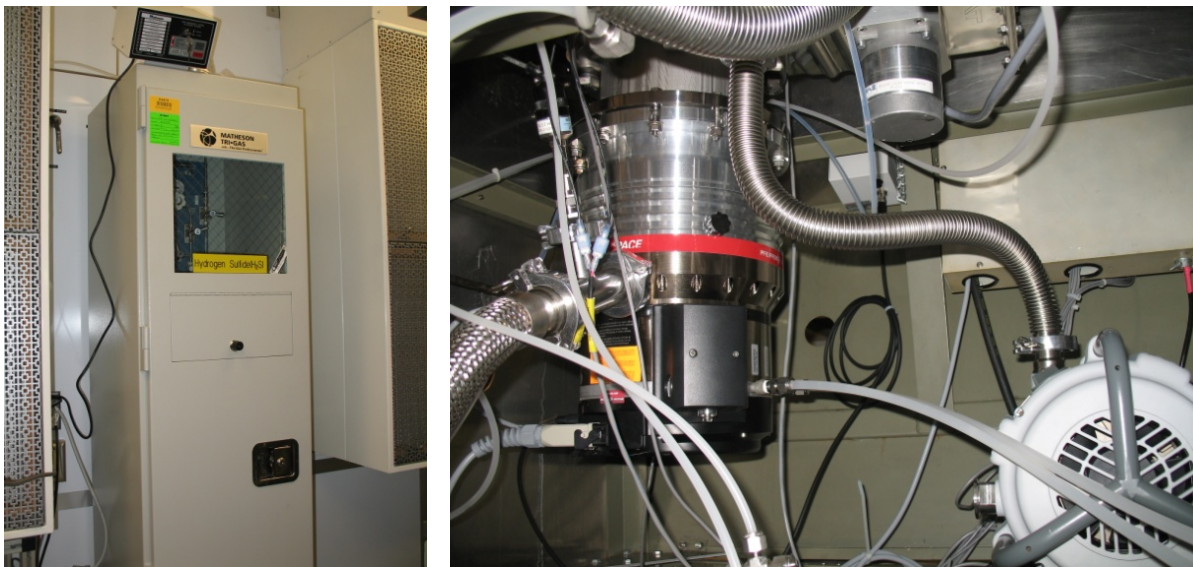


**Figure 6-2 – $H_2S$ gas cabinet and turbo-molecular pump**

Initial results with the introduction of hydrogen sulfide to the process gas (argon) are shown in Table 3. At room temperature, both 5% and 10% $H_2S$ in argon resulted in an excess of sulfur in the film suggesting the formation of a $MoS_3$ phase, which is known to be thermodynamically unstable. Increasing the substrate temperature in combination with the $H_2S$ gas resulted in the more thermodynamically stable $MoS_2$ phase with a measured S/Mo ratio of 1.97.

**Table 3 – EPMA Composition Results w/ $H_2S$**

| Run# | Description | S/Mo Ratio | Wt% Au |
|------|-------------|------------|--------|
| C174 | $MoS_2$ @ RT w/10% $H_2S$ | 2.78 | 0.0% |
| C178 | $MoS_2$ @ RT w/5% $H_2S$ | 2.68 | 0.0% |
| C179 | $MoS_2$ @ 200°C w/5% $H_2S$ | 1.97 | 0.0% |

# 7. CONCLUSIONS

Nanocomposite thin films of $MoS_2$ and Au were synthesized by co-sputter deposition with a hot stage. Novel nanostructures were generated during co-deposition at 100, 200 and 300°C, where the $MoS_2$ planes engulfed the Au nanoparticles. A combination of surface temperature and kinetic energy from the plasma was required for the formation of the $MoS_2$ basal planes encapsulated Au nanoparticle structures nano-onion like structures. Compared with pure $MoS_2$, the $MoS_2$-Au nanocomposite films grown at elevated temperatures showed significant improvements in wear life when tested in air with 50% RH. The sputter deposition in argon atmosphere resulted in substoichiometric films with a S/Mo ratio of ~1.6. To mitigate this problem the sputter system was modified to enable processing with hydrogen sulfide gas. Near stoichiometric films were synthesized by introduction of 5% $H_2S$ into argon while keeping the substrate at 200°C.

# REFERENCES

[1]     Spalvins, T., "*A Review of Recent Advances in Solid Film Lubrication",* Journal of Vacuum Science & Technology a-Vacuum Surfaces and Films, 1987. **5**(2): p. 212-219.

[2]     Hilton, M.R. and P.D. Fleischauer, "*Applications of solid lubricant films in spacecraft",* Surface and Coatings Technology, 1992. **54-55**(1-3): p. 435-441.

[3]     Prasad, S. and J. Zabinski, "*Lubricants - Super slippery solids",* Nature, 1997. **387**(6635): p. 761-762.

[4]     Singer, I.L., J. Larsenbasse, J.N. Israelachvili, and J. Greenwood, *Solid Lubrication Processes*, in *Fundamentals of Friction : Macroscopic and Microscopic Processes*. 1992, Kluwer Academic Publ: Dordrecht. p. 237-261.

[5]     Singer, I.L., R.N. Bolster, J. Wegand, S. Fayeulle, and B.C. Stupp, "*Hertzian Stress Contribution to Low Friction Behavior of Thin $MoS_2$ Coatings",* Applied Physics Letters, 1990. **57**(10): p. 995-997.

[6]     Wahl, K.J., M. Belin, and I.L. Singer, "*A triboscopic investigation of the wear and friction of $MoS_2$ in a reciprocating sliding contact",* Wear, 1998. **214**(2): p. 212-220.

[7]     Donnet, C. and A. Erdemir, "*Solid lubricant coatings: recent developments and future trends",* Tribology Letters, 2004. **17**(3): p. 389-397.

[8]     Lince, J.R., "*Tribology of co-sputtered nanocomposite $Au/MoS_2$ solid lubricant films over a wide contact stress range",* Tribology Letters, 2004. **17**(3): p. 419-428.

[9]     Hamilton, M.A., L.A. Alvarez, N.A. Mauntler, N. Argibay, R. Colbert, D.L. Burris, C. Muratore, A.A. Voevodin, S.S. Perry, and W.G. Sawyer, "*A Possible Link Between Macroscopic Wear and Temperature Dependent Friction Behaviors of $MoS_2$ Coatings",* Tribology Letters, 2008. **32**(2): p. 91-98.

[10]    Scharf, T.W., S.V. Prasad, M.T. Dugger, P.G. Kotula, R.S. Goeke, and R.K. Grubbs, "*Growth, structure, and tribological behavior of atomic layer-deposited tungsten disulphide solid lubricant coatings with applications to MEMS",* Acta Materialia, 2006. **54**(18): p. 4731-4743.

[11]    Martin, J.M., C. Donnet, T. Lemogne, and T. Epicier, "*Superlubricity of Molybdenum-Disulfide",* Physical Review B, 1993. **48**(14): p. 10583-10586.

[12]    Lince, J.R., M.R. Hilton, and A.S. Bommannavar, "*Oxygen Substitution in Sputter-Deposited $MoS_2$ Films Studied by Extended X-Ray Absorption Fine-Structure, X-Ray Photoelectron-Spectroscopy and X-Ray-Diffraction",* Surface & Coatings Technology, 1990. **43-4**(1-3): p. 640-651.

[13]    Rai, A.K., R.S. Bhattacharya, J.S. Zabinski, and K. Miyoshi, "*A comparison of the wear life of as-deposited and ion-irradiated $WS_2$ coatings",* Surface & Coatings Technology, 1997. **92**(1-2): p. 120-128.

[14]    Prasad, S.V., J.S. Zabinski, and N.T. McDevitt, "*Friction Behavior of Pulsed Laser Deposited Tungsten Disulfide Films",* Tribology Transactions, 1995. **38**(1): p. 57-62.

[15]    Voevodin, A.A., T.A. Fitz, J.J. Hu, and J.S. Zabinski, "*Nanocomposite tribological coatings with "chameleon" surface adaptation",* Journal of Vacuum Science & Technology a-Vacuum Surfaces and Films, 2002. **20**(4): p. 1434-1444.

[16]     Muratore, C. and A.A. Voevodin, *Chameleon Coatings: Adaptive Surfaces to Reduce Friction and Wear in Extreme Environments*, in *Annual Review of Materials Research*. 2009. p. 297-324.

[17]     Teer, D.G., "*New solid lubricant coatings*," Wear, 2001. **251**(1-12): p. 1068-1074.

[18]     Fox, V., A. Jones, N.M. Renevier, and D.G. Teer, "*Hard lubricating coatings for cutting and forming tools and mechanical components*," Surface & Coatings Technology, 2000. **125**(1-3): p. 347-353.

[19]     Renevier, N.M., V.C. Fox, D.G. Teer, and J. Hampshire, "*Coating characteristics and tribological properties of sputter-deposited $MoS_2$/metal composite coatings deposited by closed field unbalanced magnetron sputter ion plating*," Surface & Coatings Technology, 2000. **127**(1): p. 24-37.

[20]     Renevier, N.M., J. Hamphire, V.C. Fox, J. Witts, T. Allen, and D.G. Teer, "*Advantages of using self-lubricating, hard, wear-resistant $MoS_2$-based coatings*," Surface and Coatings Technology, 2001. **142-144**(0): p. 67-77.

[21]     Savan, A., M.C. Simmonds, Y. Huang, C.P. Constable, S. Creasey, Y. Gerbig, H. Haefke, and D.B. Lewis, "*Effects of temperature on the chemistry and tribology of co-sputtered MoSx-Ti composite thin films*," Thin Solid Films, 2005. **489**(1-2): p. 137-144.

[22]     Nainaparampil, J.J., A.R. Phani, J.E. Krzanowski, and J.S. Zabinski, "*Pulsed laser-ablated $MoS_2$-Al films: friction and wear in humid conditions*," Surface & Coatings Technology, 2004. **187**(2-3): p. 326-335.

[23]     Holbery, J.D., E. Pflueger, A. Savan, Y. Gerbig, Q. Luo, D.B. Lewis, and W.D. Munz, "*Alloying $MoS_2$ with Al and Au: structure and tribological performance*," Surface & Coatings Technology, 2003. **169**: p. 716-720.

[24]     Mikhailov, S., A. Savan, E. Pfluger, L. Knoblauch, R. Hauert, M. Simmonds, and H. Van Swygenhoven, "*Morphology and tribological properties of metal (oxide) $MoS_2$ nanostructured multilayer coatings*," Surface & Coatings Technology, 1998. **105**(1-2): p. 175-183.

[25]     Hilton, M.R., G. Jayaram, and L.D. Marks, "*Microstructure of cosputter-deposited metal- and oxide-$MoS_2$ solid lubricant thin films*," Journal of Materials Research, 1998. **13**(4): p. 1022-1032.

[26]     Lince, J.R., M.R. Hilton, and A.S. Bommannavar, "*Metal Incorporation in Sputter-Deposited $MoS_2$ Films Studied by Extended X-Ray-Absorption Fine-Structure*," Journal of Materials Research, 1995. **10**(8): p. 2091-2105.

[27]     Wahl, K.J., L.E. Seitzman, R.N. Bolster, and I.L. Singer, "*Low-Friction, High-Endurance, Ion-Beam-Deposited Pb-Mo-S Coatings*," Surface & Coatings Technology, 1995. **73**(3): p. 152-159.

[28]     Wahl, K.J., D.N. Dunn, and I.L. Singer, "*Wear behavior of Pb-Mo-S solid lubricating coatings*," Wear, 1999. **230**(2): p. 175-183.

[29]     Zabinski, J.S., M.S. Donley, V.J. Dyhouse, and N.T. McDevitt, "*Chemical and Tribological Characterization of PbO-$MoS_2$ Films Grown by Pulsed Laser Deposition*," Thin Solid Films, 1992. **214**(2): p. 156-163.

[30]     Zabinski, J.S., M.S. Donley, S.D. Walck, T.R. Schneider, and N.T. McDevitt, "*The Effects of Dopants on the Chemistry and Tribology of Sputter-Deposited $MoS_2$ Films*," Tribology Transactions, 1995. **38**(4): p. 894-904.

[31]     Scharf, T.W., P.G. Kotula, and S.V. Prasad, "*Friction and wear mechanisms in $MoS_2$/$Sb_2O_3$/Au nanocomposite coatings*," Acta Materialia, 2010. **58**(12): p. 4100-4109.

[32] Centers, P.W., "*Tribological Performance of MoS$_2$ Compacts Containing MoO$_3$, Sb$_2$O$_3$ Or MoO$_3$ And Sb$_2$O$_3$",* Wear, 1988. **122**(1): p. 97-102.

[33] Zabinski, J.S., M.S. Donley, and N.T. McDevitt, "*Mechanistic Study of the Synergism Between Sb$_2$O$_3$ and MoS$_2$ Lubricant Systems using Raman-Spectroscopy",* Wear, 1993. **165**(1): p. 103-108.

[34] Hu, J.J., J.E. Bultman, and J.S. Zabinski, "*Microstructure and lubrication mechanism of multilayered MoS$_2$/Sb$_2$O$_3$ thin films",* Tribology Letters, 2006. **21**(2): p. 169-174.

[35] Zabinski, J.S., J.E. Bultman, J.H. Sanders, and J.J. Hu, "*Multi-environmental lubrication performance and lubrication mechanism of MoS$_2$/Sb$_2$O$_3$/C composite films",* Tribology Letters, 2006. **23**(2): p. 155-163.

[36] Tenne, R., L. Margulis, M. Genut, and G. Hodes, "*Polyhedral and Cylindrical Structures of Tungsten Disulfide ",* Nature, 1992. **360**(6403): p. 444-446.

[37] Margulis, L., G. Salitra, R. Tenne, and M. Talianker, "*Nested Fullerene-Like Structures",* Nature, 1993. **365**(6442): p. 113-114.

[38] Frey, G.L., S. Elani, M. Homyonfer, Y. Feldman, and R. Tenne, "*Optical-absorption spectra of inorganic fullerenelike MS$_2$ (M=Mo, W)",* Physical Review B, 1998. **57**(11): p. 6666.

[39] Buffat, P. and J.P. Borel, "*Size Effect on Melting Temperature of Gold Particles",* Physical Review A, 1976. **13**(6): p. 2287-2298.

[40] Reich, M., S. Utsunomiya, S.E. Kesler, L.M. Wang, R.C. Ewing, and U. Becker, "*Thermal behavior of metal nanoparticles in geologic materials",* Geology, 2006. **34**(12): p. 1033-1036.

# DISTRIBUTION